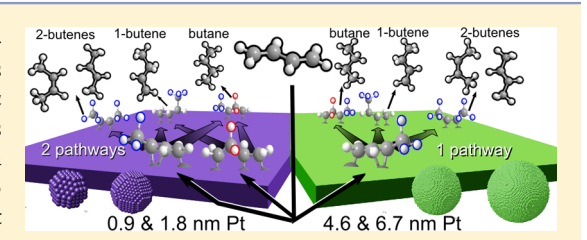# Structure Sensitivity in Pt Nanoparticle Catalysts for Hydrogenation of 1,3-Butadiene: *In Situ* Study of Reaction Intermediates Using SFG Vibrational Spectroscopy

William D. Michalak,*[,†,‡] James M. Krier,[†,‡] Kyriakos Komvopoulos,[§] and Gabor A. Somorjai*[,†,‡]

[†]Chemical Sciences and Material Sciences Divisions, Lawrence Berkeley National Laboratory, Berkeley, California 94720, United States

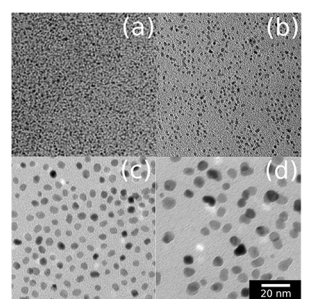[‡]Department of Chemistry, University of California, Berkeley, California 94720, United States

[§]Department of Mechanical Engineering, University of California, Berkeley, California 94720, United States

S *Supporting Information*

ABSTRACT: The product selectivity during 1,3-butadiene hydrogenation on monodisperse, colloidally synthesized, Pt nanoparticles was studied under reaction conditions with kinetic measurements and *in situ* sum frequency generation (SFG) vibrational spectroscopy. SFG was performed with the capping ligands intact in order to maintain nanoparticle size by reduced sintering. Four products are formed at 75 °C: 1-butene, *cis*-2-butene, *trans*-2-butene, and *n*-butane. Ensembles of Pt nanoparticles with average diameters of 0.9 and 1.8 nm exhibit a ~30%

and ~20% increase in the full hydrogenation products, respectively, as compared to Pt nanoparticles with average diameters of 4.6 and 6.7 nm. Methyl and methylene vibrational stretches of reaction intermediates observed under working conditions using SFG were used to correlate the stable reaction intermediates with the product distribution. Kinetic and SFG results correlate with previous DFT predictions for two parallel reaction pathways of 1,3-butadiene hydrogenation. Hydrogenation of 1,3-butadiene can initiate with H-addition at internal or terminal carbons leading to the formation of 1-buten-4-yl radical (metallocycle) and 2-buten-1-yl radical intermediates, respectively. Small (0.9 and 1.8 nm) nanoparticles exhibited vibrational resonances originating from both intermediates, while the large (4.6 and 6.7 nm) particles exhibited vibrational resonances originating predominately from the 2-buten-1-yl radical. This suggests each reaction pathway competes for partial and full hydrogenation and the nanoparticle size affects the kinetic preference for the two pathways. The reaction pathway through the metallocycle intermediate on the small nanoparticles is likely due to the presence of low-coordinated sites.

INTRODUCTION

Catalysts that promote selective hydrogenation of unsaturated hydrocarbons to mono-olefins, while inhibiting full hydrogenation, are important to the chemical industry. Active hydrogenation catalysts like Pt, however, convert 1,3-butadiene (1,3-BD, a prototype diene) into four primary products: three partial hydrogenation products (1-butene, *trans*-2-butene, and *cis*-2-butene) and one full hydrogenation product (*n*-butane). Partial hydrogenation products are produced at ~65−90% with the remainder being *n*-butane.[1−4] Experimental studies using metallic single crystals,[1,2,4,5] metal particles supported on metal oxides,[3,6] and DFT-based theoretical approaches[7−9] have been used to understand the factors that control the product distribution. One interpretation of the behavior is ascribed to the different adsorption energies of 1,3-BD and the butenes.[9] In this case, butenes readsorb and participate in secondary reactions to form *n*-butane. An alternative interpretation that is based on theoretical work suggests that a metallocycle reaction intermediate is responsible for this behavior.[8] The DFT results suggest that the full hydrogenation product observed on Pt can be attributed to a particular C_4H_8 metallocycle intermediate, which is relatively stable and evolves

into *n*-butane. The activation barrier for the formation of the metallocycle intermediate on Pt was comparable to the activation barriers that lead to the formation of the butene products. Thus, *n*-butane is believed to form simultaneously with the butenes. The results presented in this paper show that Pt nanoparticles catalyze the formation of *n*-butane and the partial hydrogenation products simultaneously through parallel pathways that initiate with different radical intermediates.

Studies using single crystals have shown that the crystal face affects adsorbate stability and transition state geometries on the surface.[10] For example, different distributions of benzene and cyclohexane are produced from cyclohexene hydrogenation at constant temperature on Pt(100) and Pt(111) surfaces because of the differences in stability of 1,3-cyclohexadiene and 1,4-cyclohexadiene reaction intermediates.[11] Product distribution is also affected by the size of metal nanoparticle catalysts, which produce different geometric and electronic effects.[5,12−16] Geometric effects include the distribution of kinks, steps, and terrace sites exposed on the catalyst surface, whereas electronic

effects include variations in the d-band center and width and the electronic screening effects that the adsorbate experiences as the ratio of surface atoms to bulk atoms approaches one. Studies using colloidally prepared Pt metal nanoparticles have demonstrated that the product distribution can vary significantly in the 1−10 nm size range where the electronic and geometric factors play a role (e.g., refs 17−19).

The objective of this study was to examine the size effect of Pt nanoparticle catalysts on the product distribution during hydrogenation of 1,3-BD. We show that monodisperse ensembles of polyhedral Pt nanoparticle catalysts with 0.9 and 1.8 nm average diameter exhibit changes in selectivity for *n*-butane and 1-butene as compared to Pt nanoparticles of 4.6 or 6.7 nm average diameter. Molecular-level studies were performed with the system under reaction conditions with *in situ* sum frequency generation (SFG) vibrational spectroscopy, which exclusively probes adsorbed intermediates. We perform SFG on nanoparticle catalysts with ligand capping agents intact so that sintering is avoided and the particle size is maintained.

■ EXPERIMENTAL SECTION

1. Materials. Hexachloroplatinic acid ($H_2PtCl_6 \cdot 6H_2O$, 99%), poly(vinylpyrrolidone) (PVP, MW = 29 000 amu), ethylene glycol (reagent grade), HCl (2 M), 1,3-butadiene (99%), and NaOH (99.9%) were manufactured by Sigma-Aldrich. Hydrogen (5.0 UHP), helium (5.0 UHP), and Ar (5.0 UHP) were purchased from Praxair. Polished silicon (100) wafers were purchased from Addison Engineering.

2. Nanoparticle Synthesis. Polyhedral platinum nanoparticles of average diameter in the range of 0.9−7 nm were prepared using polyol methods described in the literature,[19] with PVP capping ligands to prevent aggregation. Details of the syntheses are given in the Supporting Information. The nanoparticles were separated from the postsynthesis colloidal suspension by precipitation with acetone and centrifugation at 4000 rpm (VWR, Clinical 50) for 5 min. Further washing with ethanol and hexane was performed up to seven times to remove residual molecular fragments from the particle surface. The nanoparticles were stored in ethanol under refrigeration until their use in kinetic and spectroscopic studies.

3. Langmuir−Blodgett Film Deposition. For both kinetic and spectroscopic studies, the nanoparticles were supported on a silica surface because it is an inert, low acidity surface that guarantees negligible activity. The use of a two-dimensional support differs from common catalytic studies that use high surface area materials (e.g., silica, alumina, or carbon) as catalyst supports. We cannot use the high surface area three-dimensional supports because SFG spectroscopy requires that incoming and outgoing photons are in direct line-of-sight with molecules adsorbed on the surface of the catalyst and photodetector, respectively. Pt nanoparticles were deposited onto a silicon wafer (Si(100)) that was prepared with 5000 Å thick thermal oxide layer (kinetic studies) or a fused silica prism (spectroscopic studies) using a Langmuir−Blodgett (LB) trough (Kibron, MTX). Before nanoparticle deposition, the silica surfaces were exposed to strong oxidizers (e.g., piranha or NoChromix) to remove organic residues and make them hydrophilic (oxidizers hydroxylate the silica). Nanoparticles were dispersed in chloroform and deposited onto an ultrapure water subphase (18.2 MΩ·cm). Following the evaporation of chloroform and equilibration of particles (30−60 min), the two-dimensional layer of particles was compressed at a rate of 10 mm/min to create a close-packed monolayer. When the monolayer of particles was compressed to a surface pressure in the range of 30−35 mN/m, the substrates were withdrawn at a rate of 2 mm/min while at constant pressure. Surface tension was monitored using a Wilhelmy probe made of a PtIr wire.

4. Materials Characterization. Nanoparticle morphology and size were examined using a transmission electron microscope (TEM, JEOL 200CX) operated at 120 kV. The images shown in Figure 1
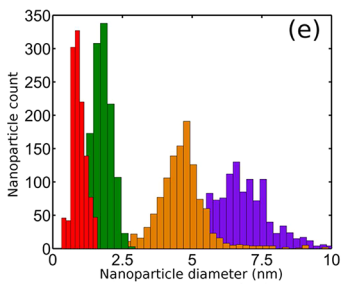

Figure 1. Transmission electron microscopy images of polyhedral Pt nanoparticles. Panels a, b, c, and d show nanoparticles with an average diameter and standard deviation of 0.94 ± 0.26, 1.80 ± 0.34, 4.63 ± 1.12, and 6.67 ± 1.20 nm, respectively. Panel e shows particle size distributions for the four particle sizes. The 20 nm scale bar in panel d reflects the scale for all images.

demonstrate the morphology and size of nanoparticles with an average diameter of 0.94 ± 0.26, 1.80 ± 0.34, 4.63 ± 1.12, and 6.67 ± 1.20 nm. The monodispersity of the nanoparticles is demonstrated by the nanoparticle size distributions shown in Figure 1e, which were obtained with >300 particles using ImageJ software.

5. Kinetic Measurements. Hydrogenation reactions were performed in a 1 L stainless steel chamber equipped with a capacitance manometer pressure gauge (MKS Baratron), a metal bellows recirculating pump (Senior Aerospace MB-21), a turbomolecular pump (Pfeiffer), and a mechanical rotary pump. Conflat flanges with Cu gaskets were used to seal the reaction chamber. The temperature of the sample was maintained by resistively heating a boronitride ceramic plate (Momentive) and monitored using a type K thermocouple. The conversion of 1,3-butadiene to 1-butene, *cis*-2-butene, *trans*-2-butene, and *n*-butane was monitored using a gas chromatograph (Shimadzu GC-17A, Agilent Plot Alumina "S" capillary column (0.2 mm × 30 m)) equipped with a flame ionization detector. Prior to each reaction, the chamber was evacuated using the turbomolecular pump. The gate valve to the pumps was closed prior to introducing the reactant species. Selectivities were calculated by comparing the rate of accumulation for each species at a conversion of 1,3-BD of <10%. Blank experiments in the absence of Pt nanoparticles indicated negligible background activity.

6. Sum Frequency Generation Vibrational Spectroscopy. Details regarding the theory of SFG can be found elsewhere.[20−22] Briefly, SFG vibrational spectroscopy relies on a nonlinear optical phenomenon that occurs when two pulsed laser beams—with visible and infrared frequencies—overlap. The selection rules for SFG activity maintain that the excited molecular resonance is in an asymmetric environment (i.e., an interface), and the molecules have a net polar orientation. The first requirement indicates that the SFG process can only occur in a medium without centrosymmetry (i.e., an interface). Thus, neither the Pt nanoparticle bulk nor the gas phase mixture will yield spectroscopic signatures and only the *z*-component of molecules at an interface will produce a SFG signal. The second requirement indicates that no photon emission is detected from species arranged in an equal number of opposite orientations on a surface or from a completely disordered surface structure.[22] Therefore, the SFG intensity is a function of both the concentration of interfacial species and their orientation.

SFG vibrational spectroscopy was performed with a mode-locked Nd:YAG dye laser (Continuum D-20) with 1064 nm fundamental output, 20 Hz repetition rate, and 20 ps pulse width. A frequency-doubling crystal was used to generate a visible (532 nm) beam from the fundamental beam. An optical parametric generator/amplifier produced tunable infrared in the 2680−3180 cm[1] range, corresponding to the stretching modes of aliphatic and aromatic groups. Visible and infrared beams of 130 μJ power were spatially and temporally overlapped at the base of a polished fused silica equilateral (60°) prism (ISP Optics) at angles of 63° and 48°, respectively, from the surface normal to achieve total internal reflection. All of the experiments were

performed in ppp polarization combination. SFG photons were detected by a photomultiplier tube with a gated boxcar integrator.

In situ SFG spectroscopy experiments were performed by mounting the optical prism onto a batch reactor as described previously.[23] Nanoparticles directly deposited onto the prism using the LB trough were simultaneously exposed to the gas phase mixture and the visible and IR evanescent waves, which were produced by total internal reflection. We ensured a closed environment by sealing the prism/reactor interface with a Kalrez O-ring. The reaction temperature and gas pressures were identical to the kinetic studies with the exception that the inert gas was Ar instead of He.

Quantitative analysis of the relative peak intensities in SFG spectroscopy requires an understanding of the IR and Raman transitions of the molecules on the surface and the interferences between the nonresonant and resonant contributions. The SFG intensity, I_{SFG}, can be described by

$$I_{SFG} \propto \left| \chi_{NR}^{(2)} e^{i\varphi_{NR}} + \sum_{\nu} \left(\frac{A_{\nu} e^{i\delta_{\nu}}}{\omega_{\nu} - \omega_{IR} + i\Gamma_{\nu}} \right) \right|^2 I_{vis} I_{IR} \tag{1}$$

where I_{vis} and I_{IR} are the intensities of the incident visible and infrared photons, respectively, and $\chi_{NR}^{(2)}$ and φ_{NR} are the magnitude and phase change (relative to the incident beam) of the nonresonant susceptibility, respectively. The term in eq 1 with the summation equals the resonant susceptibility ($\chi_{R,\nu}^{(2)}$) corresponding to the νth vibrational mode; A_{ν}, ω_{ν}, δ_{ν}, and Γ_{ν}^{-1} are the magnitude, frequency, phase change, and the relaxation time of the vibrationally excited state involved in vibrational resonance, respectively.[22] For analysis of the SFG spectra as a function of nanoparticle size, the SFG spectra were decomposed according to eq 1, and the quantity used for the evaluation of the intensity, I_{ν}, is given by

$$I_{\nu} = \int_{-\infty}^{\infty} \left| \frac{A_{\nu}}{\omega_{\nu} - \omega_{IR} + i\Gamma_{\nu}} \right|^2 d\omega_{IR} = \frac{A_{\nu}^2}{\Gamma_{\nu}} \tag{2}$$

as performed in a previous study.[24] Because the net intensity of the SFG spectra varies on different nanoparticles, we normalize by the sum of all measured intensities ($\hat{I}_{\nu} = I_{\nu} / \sum_i I_{\nu_i}$) when comparing spectra from Pt nanoparticles of different sizes.

Curve fitting was performed with Matlab using a constrained sequential quadratic programming optimization algorithm (fmincon)[25] in conjunction with a multistart framework to find the global minimum (globalsearch).[26] Prior to performing the fitting routine, I_{SFG} was normalized by a factor equal to the average over the IR intensities entering the prism and leaving the prism (as a function of ω_{IR}). During the fitting routine, the phase terms, φ_{NR} and δ_{ν}, were constrained to values between $-\pi$ and π, while the remaining terms in eq 1 were constrained to positive values.

7. Detecting Reaction Intermediates in the Presence of PVP Capping via H_2-Induced Disordering. Catalysts prepared by colloidal synthesis techniques use organic ligand molecules to "cap" the nanoparticles. The capping agent prevents agglomeration during synthesis and under reaction conditions when the nanoparticles are exposed to high temperatures.[27] Separating the signal of the reaction intermediates from the signal of the capping agent can be challenging. However, we recently demonstrated that for PVP-capped Pt nanoparticles the presence of gas-phase H_2 disorders PVP and reduces its signal intensity.[28] An example of SFG spectra demonstrating this behavior is shown in Figure S1 (Supporting Information). With the SFG signal from PVP significantly reduced, the signal from the reaction intermediates during 1,3-BD hydrogenation was detected without interference from the capping material.

8. Hazards. Caution should be taken when using 1,3-butadiene, which is a known carcinogen and teratogen. SFG uses Class 4 lasers that are potentially hazardous to the eyes and skin.

■ RESULTS

Hydrogenation of 1,3-butadiene (1,3-BD) was performed on ensembles of Pt nanoparticle catalysts with average diameters

equal to 0.94, 1.80, 4.63, and 6.67 nm. The reaction was performed at a constant temperature of 75 °C using a reactant gas mixture composed of 10 Torr of 1,3-BD, 100 Torr of H_2, and 650 Torr of inert gas (He and Ar for kinetic and spectroscopic studies, respectively). Reaction intermediates were measured under reaction conditions using SFG spectroscopy. We correlate the kinetic and spectroscopic results with the theoretical results obtained by Sautet and co-workers.[7−9] Following is a brief description of their predicted reaction intermediates.

1. Predicted Reaction Intermediates of 1,3-Butadiene Hydrogenation. Hydrogenation of 1,3-BD (C_4H_6) is a chemical reaction that includes the formation of a C_4H_7, C_4H_8, C_4H_9, and C_4H_{10} species through the stepwise addition of H atoms (Figure 2). According to DFT-based computational
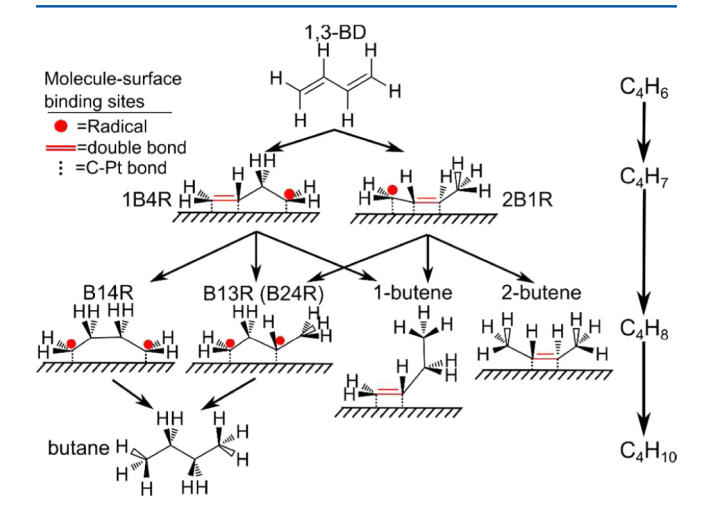

Figure 2. Schematic of reaction pathways for 1,3-butadiene (1,3-BD) hydrogenation, DFT-predicted stable intermediates during hydrogenation, and observed products. Addition of the first H atom leads to 1-buten-4-yl radical (1B4R) or 2-buten-1-yl radical (2B1R); addition of a second H atom leads to butan-1,4-diyl radical (B14R), butan-1,3-diyl radical (B13R) or butan-2,4-diyl (B24R) intermediates, or 1-butene (1B) and 2-butene (2B) products. The nomenclature corresponds to IUPAC gas-phase radicals, in which an "R" designates a radical. Carbon radicals and double bonds that are highlighted in red designate their locations in the gas phase, which correspond to the locations of C−Pt bonds that are shown by dotted lines. The reaction intermediates shown are based on the DFT predictions of Valcarcel et al.[8]

studies of Sautet and co-workers,[7−9] there are six stable reaction intermediates for 1,3-BD on Pt(111). The most stable chemisorbed structure of 1,3-BD on Pt is a tetra-σ binding geometry. Addition of the first H atom to a terminal carbon (C_1 or C_4) of a tetra-σ intermediate produces the 2-buten-1-yl radical (2B1R) and H-addition to an internal carbon (C_2 or C_3) produces the 1-buten-4-yl radical (1B4R). The nomenclature used here follows the IUPAC conventions for gas-phase radicals as practiced by Valcarcel et al.:[8] the first number accounts for the position of the "remaining" double bond, and the second number(s) accounts for the position of the radical C atom(s). The intermediates discussed here are not actually radicals but are strongly bound closed-shell complexes; the terminology is used only for classification purposes. The 1B4R has three σ-bonds at the C_1, C_2, and C_4 atoms. The 2B1R is a methylallyl that has one σ-bond with Pt at the C_1 atom and one π-bond with a Pt atom shared across the C_2 and C_3 atoms.

For each C_6H_7 species, there are three possibilities to add a second H atom. H-addition to 1B4R at the C_1 atom produces a butan-2,4-diyl radical (B24R), the C_2 atom produces a butan-1,4-diyl radical (B14R), and the C_4 atom produces 1-butene. H-addition to 2B1R at the C_1 atom produces 2-butene, the C_2 atom produces a butan-1,3-diyl radical (B13R), and the C_3 atom produces 1-butene. The B13R and B24R are equivalent species even though they are obtained through different pathways. Only the B14R or B13R (or B24R) species can directly lead to n-butane from 1,3-BD via addition of two additional H atoms. The stable gas-phase products include three C_4H_8 species (1-butene, cis-2-butene, and $trans$-2-butene) and one C_4H_{10} species (n-butane).

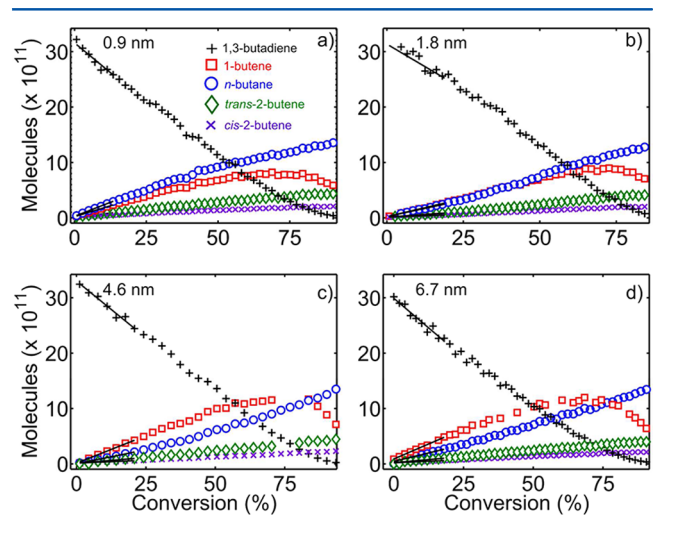## 2. Role of Nanoparticle Size for 1,3-Butadiene Hydrogenation. Figure 3 shows the number of molecules of

Figure 3. Number of molecules versus percent conversion for (+) 1,3-butadiene hydrogenation (T = 75 °C, 10 Torr of 1,3-BD, 100 Torr of H_2, 650 Torr of He) over ensembles of Pt nanoparticles with average diameters of (a) 0.9, (b) 1.8, (c) 4.6, and (d) 6.7 nm. The products include 1-butene (□), n-butane (○), $trans$-2-butene (◇), and cis-2-butene (×). Black lines indicate the linear regions that are used to calculate the selectivity.

1,3-BD converted over the Pt catalysts and the number of produced molecules of n-butane, 1-butene, $trans$-2-butene, and cis-2-butene produced versus total 1,3-BD conversion for different nanoparticle sizes. All four species were produced, and no C−C coupling or C−C scission products were observed regardless of nanoparticle size. The formation rates of n-butane and 1-butene are nearly equal at low conversion for both 0.9 and 1.8 nm Pt nanoparticles; however, the larger size nanoparticles (4.6 and 6.7 nm) exhibit the preferential formation of 1-butene. When 1,3-BD reaches ∼75% conversion, the concentration of 1-butene in the batch reactor stops increasing and then decreases due to a secondary reaction to n-butane for all size nanoparticles. This behavior indicates that in the presence of excess 1,3-BD the 1-butene or 2-butene does not competitively readsorb. In all cases, $trans$-2-butene and cis-2-butene are minor products and are formed at a rate that is independent of 1,3-BD concentration.

Product selectivity to the four products was calculated using the ratio of formation rates at conversion below 10% (black lines in Figure 3). Figure 4 shows the product selectivity distributions with ensembles of Pt nanoparticle catalysts of different sizes. The dashed lines are used to indicate trends. Pt
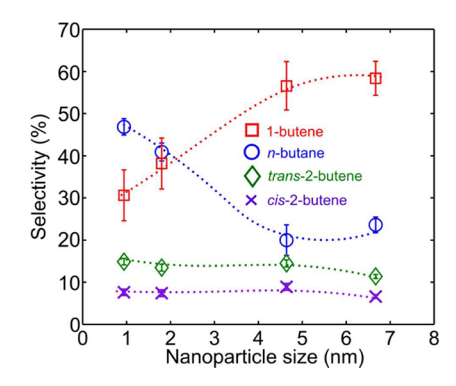

Figure 4. Product selectivity for 1-butene (□), n-butane (○), $trans$-2-butene (◇), and cis-2-butene (×) from the conversion of 1,3 butadiene (1,3-BD) hydrogenation (T = 75 °C with 10 Torr of 1,3-BD, 100 Torr of H_2, and 650 Torr of He) as a function of nanoparticle size.

nanoparticle catalysts with an average diameter of 6.7 nm yielded 80% butenes (partial hydrogenation) and 20% n-butane (full hydrogenation). The distribution of butenes was also split 80:20 for 1-butene versus 2-butene with $trans$- and cis-2-butene contributing 15% and 5% to the total. The product distribution observed for the 6.7 nm particles was similar to that observed on bulk Pt single crystals ((111) and (100)) and foils in the temperature range 25−125 °C.[2,4] In these former studies, the butenes were produced with 60−87% selectivity and a distribution of 1-butene and 2-butenes in ratios of 70−80% and 30−20%, respectively. Pt nanoparticle catalysts with an average particle diameter of 4.6 nm yield a partial to full hydrogenation product ratio that remains similar to the 6.7 nm particles (80:20). Pt nanoparticles with an average particle size of 1.8 and 0.9 nm yield a partial to full hydrogenation product ratio of 40:60 and 47:53, respectively. This corresponds to a net decrease of ∼30% for the butenes from 6.7 to 0.9 nm nanoparticle ensembles. As the particle size decreases, the ratio of 2-butene gives a slight preference to $trans$-2-butene, yet the change is insignificant. Thus, the increase in n-butane production with decreasing nanoparticle size occurred at the expense of 1-butene production.

The similar selectivity of the 6.7 nm particles with those of the bulk measurements suggests that the capping agent (PVP) does not play a role in the catalytic process. To further confirm the negligible role of PVP, we performed UV-treatment of the nanoparticles under ambient atmosphere for 1 h. This treatment has been shown to effectively degrade PVP.[23,28] The product distribution of the treated particles to n-butane, 1-butene, $trans$-2-butene, and cis-2-butene was 23%, 58%, 11%, and 6%, respectively. The similar selectivity between the treated and untreated 6.7 nm nanoparticles (only the latter are shown in Figure 4) confirms that PVP ligands do not participate in the catalytic reaction.

Kinetic results for the hydrogenation of 1,3-BD on Pt nanoparticles confirm that the product selectivity is indeed structure sensitive, that is, nanoparticle size dependent. The general trend was an increased selectivity to full hydrogenation products as the size of nanoparticle ensembles decreased, accompanied by a slight increase in $trans$-2-butene production. The kinetic selectivity trend suggests that there is an inherent difference in the reaction pathways for 1,3-BD hydrogenation on Pt nanoparticles of various sizes. To elucidate the observed selectivity differences, we use $in situ$ SFG vibrational spectros-

copy to monitor the stable reaction intermediates with different size nanoparticles.

3. *In-Situ* Detection of the Reaction Intermediates in 1,3-Butadiene Hydrogenation by SFG Vibrational Spectroscopy. SFG vibrational spectroscopy is a surface specific technique that exclusively probes molecules at interfaces. The interface specificity provides a means to probe the most stable, or long-lived, intermediate(s) adsorbed on a catalyst's surface under reaction conditions without interference from gas phase molecules. We used *in situ* SFG during 1,3-BD hydrogenation at a constant temperature of 75 °C and a reactant gas mixture composed of 10 Torr of 1,3-BD, 100 Torr of H_2, and 650 Torr of Ar. To determine whether the changes in reaction selectivity on Pt nanoparticle catalysts correspond to alternate reaction pathways, we measured the aliphatic region of the vibrational spectrum to probe the methyl, methylene, methylidyne, and vinylic groups of stable reaction intermediates. The aliphatic region of the vibrational spectrum for linear hydrocarbons is complicated by the variety of conformers and reaction pathways that exist due to the rotational degrees of freedom accompanying the C−C bond. Moreover, all unsaturated and partially saturated intermediates present on the Pt surface during 1,3-BD hydrogenation comprise methyl, methylene, methylidyne, or vinylic groups. Therefore, an understanding of the possible reaction intermediates, associated reaction pathways, and the vibrational resonances that are expected from those intermediates is essential to the interpretation of the SFG results. In addition, correctly assessing the *in situ* SFG results requires an understanding that intermediates with the longest lifetime dominate the SFG signal regardless of whether they are spectator species or reactive intermediates. To determine whether the SFG signal arises from spectator or reactive species, the SFG signal was collected upon exposing the surface to the reaction mixture followed by evacuation of the reaction chamber and reintroduction of H_2. If the signal rapidly returned to the baseline spectra observed initially, the *in situ* SFG signal was attributed to reactive species.

Previous SFG studies regarding the adsorption structures of ethylene,[29,30] propylene,[31] isobutene,[32] *n*-hexane, 2-methylpentane, 3-methylpentane, and 1-hexene on Pt(111)[21] and Pt(100),[33] methylfuran and dimethylfuran on Pt nanoparticles,[23] reflection−absorption infrared spectroscopy (RAIRS) studies on a series of *n*-alkanes (*n* = 3−10),[34,35] and in particular C_4 hydrocarbons[36] provide a reference for band assignments of the aliphatic vibrations. SFG and RAIRS are complementary because both techniques follow the metal surface selection rule that requires the transition dipole vector of a vibrational mode to have components normal to the surface to be active. Note that SFG also requires that a vibrational mode induces a change in the polarizability of a molecule (Raman-active), and therefore, RAIRS and SFG are not identical. Depending on the particular adsorbate configuration, methyl, methylene, and methylidyne groups will have unique SFG-active vibrational resonances. Methyl or methylene groups that are oriented away from the surface exhibit modes similar to the condensed phase stretches: symmetric methylene ($CH_2(s)$) and methyl ($CH_3(s)$) bands appear at about 2850 and 2875 cm^{-1}; asymmetric methylene ($CH_2(a)$) and methyl ($CH_3(a)$) bands appear at about 2935 and 2970 cm^{-1}; symmetric and asymmetric vinylic methylene bands (=$CH_2(s)$ and =$CH_2(a)$) appear at about 2990 and 3085 cm^{-1}, respectively; and the tertiary methylidyne C−H band appears at 2910 cm^{-1}. When methylene or methyl groups are in

the proximity of a metal surface (e.g., flat-lying adsorbate), their vibrational modes are perturbed as a consequence of charge transfer from the metal surface. The perturbation results in a red-shift and a band broadening from the condensed phase values.[36] Furthermore, the H−metal surface interaction is believed to force the vibrational modes of the atoms pointing toward the surface (down) and pointing away from the surface (up) to decouple. On Pt(111), perturbed (p) methylene bands, with H pointing toward ($CH_2(p,down)$) and away ($CH_2(p,up)$) from the surface appear at about 2670−2700 and 2900 cm^{-1}, respectively; perturbed methyl bands with H down ($CH_3(p,down)$) and pointing up ($CH_3(p,up)$) appear at about 2800−2820 and 2930−2945 cm^{-1}, respectively.[34]

The *in situ* SFG vibrational spectra of the stable reaction intermediates present during 1,3-BD hydrogenation are shown in Figure 5. Blue circles and dashed red lines are the average and standard deviation over nine SFG spectra, while solid black lines represent the best-fit model spectra. Comparison of the SFG spectra shown in Figure 5 suggests that the stable intermediates on the 0.9 and 1.8 nm particles (designated as
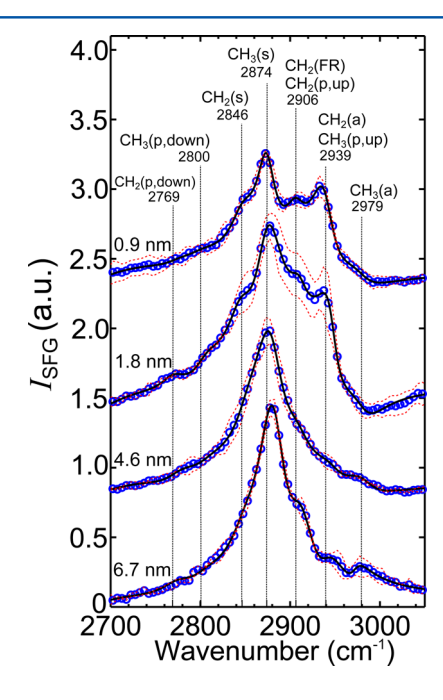

Figure 5. *In situ* SFG vibrational spectra of reaction intermediates produced on 0.9, 1.8, 4.6, and 6.7 nm Pt nanoparticle catalysts during 1,3-BD hydrogenation (*T* = 75 °C with 10 Torr of 1,3-BD, 100 Torr of H_2, and 650 Torr of Ar). Blue dots and red dashed lines represent averages and standard deviations of nine SFG spectra, respectively, while black lines represent optimized model SFG spectra using eq 1. Assignments of vibrational bands are based on model spectra (more than one mode is assigned in the case of resonances with similar peak locations). $CH_2(s)$ and $CH_2(a)$ modes appear at 2846 and 2939 cm^{-1}, while $CH_3(s)$ and $CH_3(a)$ modes appear at 2874 and 2979 cm^{-1}, respectively. Perturbed modes (*p*), reflecting C−H···Pt interactions appear for methyl and methylene groups. Perturbation causes a decoupling of the H atoms near the surface (down) and the H atoms pointing away from the surface (up). $CH_2(p,up)$ and $CH_2(p,down)$ appear at 2939 and 2769 cm^{-1}, while $CH_3(p,up)$ and $CH_3(p,down)$ appear at 2939 and 2800 cm^{-1}, respectively. Vibrational resonances below 2850 and above 2940 cm^{-1} are not visually apparent but are required to fit the spectra. In particular, an out-of-phase $CH_3(a)$ mode is required to fit the wavenumber region above 2940 cm^{-1}. Best-fit parameters for each model are given in Table S1 (Supporting Information).

Table 1. Summary of Band Assignments for the *In Situ* SFG Performed in the Presence of 10 Torr of 1,3-Butadiene, 100 Torr of H$_2$, and 650 Torr of Ar at 75 °C

location (cm^{-1})	band assignment	location (cm^{-1})	band assignment
2680	CH$_2$(p,down)[21,33,34,36]	2874	CH$_3$(s)[11,21,24,28.29−36]
2769	CH$_2$(p,down)[21,33,34,36]	2906	CH$_2$(FR)/CH$_2$(p,up)[21,34,37]
2800	CH$_3$(p,down)[21,33,34,36]	2939	CH$_2$(a)/CH$_3$(p,up)[21,34,36]
2846	CH$_2$(s)[11,21,24,28,29−36]	2979	CH$_3$(a)[11,21,24,28,29−36]

small) are similar under reaction conditions, whereas, the spectra of the 4.6 and 6.7 nm particles (designated as large) are similar but differ from those of the small particles. The small particles exhibit at least four visually apparent bands, whereas the large particles exhibit only one. The overall shape of the SFG spectra is dependent, in part, on the magnitude of each band and their phase relations. Unlike Raman and infrared vibrational spectroscopies, the magnitude of a peak is not linearly correlated with the concentration of the vibrationally active species. The nonlinear interaction between the resonant susceptibilities of each band, as well as with the nonresonant susceptibility, can give rise to constructive and destructive interference, which can augment and diminish bands. These factors can make the experimental SFG spectrum visually deceptive. We address the contributions of each band to the SFG spectra using eq 1 as a model and by optimizing over the set of parameters to provide an accurate description of the surface chemistry.

3.1. SFG Vibrational Spectra of 1,3-Butadiene Reaction Intermediates Observed on 0.9 and 1.8 nm Pt Nanoparticle Catalysts. The top two SFG spectra in Figure 5 correspond to the stable reaction intermediates of 1,3-BD hydrogenation over ensembles of small (0.9 and 1.8 nm) Pt nanoparticles. The vibrational band with the largest visually apparent magnitude at 2874 cm^{-1} is assigned to a CH$_3$(s) stretch. This band indicates that one or more of the stable reaction intermediates is bound in a standing-up, or partially standing, geometry. For example, butylidyne adsorbs with one C−Pt bond in a completely standing-up geometry, whereas 1-butene adsorbs in a partially standing geometry with di-σ bonds on the C$_1$ and C$_2$ atoms and the C$_3$−C$_4$ bond normal to the surface.[36] The other band with a clearly defined peak at 2939 cm^{-1} can be assigned to either a CH$_2$(a) on a C$_2$ (or C$_3$) internal atom or a CH$_3$(p,up) resonance on a C$_1$ (or C$_4$) terminal atom.[21,34,36] The CH$_2$(a) resonance originates from a C$_2$ or C$_3$ atom of a flat-lying intermediate such as a metallocycle, which is formed after a C atom detaches from the Pt surface following β-hydrogenation. We do not assign the CH$_2$(a) resonance to the C$_3$ atom of an adsorbed 1-butene because this methylene is equatorial, and the transition dipole vector is expected to have a negligible *z*-component. Internal methylene groups oriented in a standing geometry are also unlikely because one tenet of SFG activity is that the susceptibility tensor vanishes if C−H groups are arranged centrosymmetrically. This occurs, for example, when internal CH$_2$ groups of a hydrocarbon chain are arranged in an all-*trans* conformation, which is the stable conformation of a standing chain.[24] Given these reasons, the CH$_2$(a) originates from either the 1B4R, B14R, or B13R metallocycle intermediates.

The CH$_3$(p,up) stretch is also indicative of a semiflat-lying adsorbate that has a terminal methyl group.[34] In these configurations, the terminal methyl has H-stretches with parallel and perpendicular vector components with respect to the surface. An adsorbate with a di-σ binding geometry, in

which the C$_2$−C$_3$ atoms are attached to Pt (i.e., adsorbed 2-butene), or a π-allyl binding geometry that has a C$_1$−Pt σ-bond and C$_2$−C$_3$−Pt π-bond, will exhibit this resonance. These configurations are representative of the B13R and 2B1R adsorbed intermediates, respectively. Because each scenario is possible, we assign the band at 2939 cm^{-1} to a combination of CH$_2$(a) and CH$_3$(p,up) modes. We did not include two unique feature designations because there was insufficient spectral resolution to accurately assign peak locations with confidence.

Two other bands are visually apparent in the SFG spectra of the catalysts with 0.9 and 1.8 nm Pt nanoparticle catalysts. The shoulder at 2846 cm^{-1} at wavenumbers below the CH$_3$(s) is assigned to a CH$_2$(s) stretching mode. This resonance originates from an interior methylene (C$_2$ or C$_3$) group of a flat-lying intermediate, as described for the CH$_2$(a) stretch. The presence of the CH$_2$(s) mode, in contrast to a perturbed mode, suggests that at least one stable reaction intermediate has H atoms oriented away from the surface. The feature located between the CH$_3$(s) and CH$_2$(a)/CH$_3$(p,up) at 2906 cm^{-1} can be assigned to three possible modes or a combination thereof: a Fermi resonance (FR) that arises from the first overtone of the C−H bend of a methylene group and a fundamental methylene stretching mode (CH$_2$(FR)), a perturbed methylene stretch for the atom pointing away from the surface (CH$_2$(p,up)), or a tertiary C−H stretching mode.[21,34] We discount the possible influence of a tertiary C−H stretch because this stretch is likely equatorial. The negligible SFG activity of the tertiary C−H was demonstrated by Cremer et al., who compared the SFG vibrational signature of propylene and partially deuterated propylene (CD$_3$CHCH$_2$) adsorbed on Pt(111).[31] No peaks above 2900 cm^{-1} were observed using the deuterated species. However, both CH$_2$(FR) and CH$_2$(p,up) modes were identified in the RAIRS and SFG spectra of linear alkanes adsorbed on Pt(111).[21,34,37]

The four bands at 2846, 2874, 2906, and 2939 cm^{-1} constitute the primary, visually identifiable, spectral features of the SFG spectra for the ensembles of small nanoparticle catalysts. These are the primary bands used to correlate the observed reaction intermediates with nanoparticle size. Each band and their assigned origins are summarized in Table 1. The optimized best-fit A_ν, ω_ν, δ_ν, and Γ_ν parameters, for each of these bands, are shown in Table S1 (Supporting Information). With only these four modes, we were unable to develop a model that yielded a satisfactory fit to the experimental SFG spectra. The primary discrepancy between the model—using only these four bands—and the experimental data was the representation of the leading and tailing regions from 2700−2850 and 2940−3100 cm^{-1}. The line shape of $\chi^{(2)}_{R,q}$ is comparable to a Lorentzian.[22] A Lorentzian profile features leading and tailing edges that exhibit convex shapes, whereas the SFG spectral profiles shown for the ensembles of small nanoparticle catalysts do not. This suggests that the experimental data must have contributing resonant or non-resonant terms that exhibit constructive or destructive

interference in the leading and tailing regions. Because the conclusions from this study are not based on these additional features, their presentation is given in the Supporting Information. In summary, we predict additional features at 2680, 2769, 2800, and 2979 cm^{-1} (the feature at 2680 cm^{-1} is not shown in Figure 5). We assign the two features at 2680 and 2769 cm^{-1} to CH$_2$(p,down) modes and the features at 2800 and 2979 cm^{-1} to CH$_3$(p,down) and CH$_3$(a) modes, respectively.

3.2. SFG Vibrational Spectra of 1,3-Butadiene Reaction Intermediates Observed on 4.6 and 6.7 nm Pt Nanoparticle Catalysts. The bottom two SFG spectra in Figure 5 correspond to the stable intermediates of 1,3-BD hydrogenation on the ensembles of large (4.6 and 6.7 nm) Pt nanoparticle catalysts. These spectra exhibit a single dominant feature at ~2878 cm^{-1} (shifted 4 cm^{-1} in comparison to the spectra for the small nanoparticle catalysts). We assign this feature to a CH$_3$(s) as specified with the small particles. However, unlike the SFG spectra for the small particles, there are no other well-resolved features in the spectra. While shoulders at 2910, 2939, and 2979 cm^{-1} are present in the spectrum for the 6.7 nm particles, the spectra for the 4.6 nm particles appears as a single broad profile. A broad spectrum can be attributed to inhomogeneous broadening that is a consequence of many local environments of the adsorbate, temperature-induced broadening, and similar resonances that come from different adsorbed intermediates.[21,33,34] However, if we use a single feature to model the SFG spectra shown for the 4.6 and 6.7 nm particles, the full width half-maximum ($2\Gamma_\nu$) approximately equals 120 cm^{-1}, or a value of $\Gamma_\nu = 60$ cm^{-1}. Fundamental vibrations and perturbed modes have values in the ranges ~10−20 and 25−40 cm^{-1}, respectively.[21,24] Therefore, a single CH$_3$(s) feature is physically unreasonable. To fit the SFG spectra for the 4.6 and 6.7 nm Pt nanoparticle catalysts, we constrained $\omega_\nu \pm 10$ cm^{-1} from the optimal values of the 1.8 nm SFG spectra and allowed A_ν, δ_ν, and Γ_ν to vary with the same bounds used previously. The best-fit model spectra for the 4.6 and 6.7 nm Pt nanoparticles comprise the same features as the best-fit model spectra for the 0.9 and 1.8 nm Pt nanoparticles. On the basis of the models, we predict that the next most influential features in the SFG spectra after the dominant feature at ~2878 cm^{-1} are located at 2906 and 2979 cm^{-1}, corresponding to the CH$_2$(FR)/CH$_2$(p,up) and CH$_3$(a) resonances, respectively.

■ DISCUSSION

The combination of kinetic selectivity measurements and *in situ* vibrational spectroscopy provides a unique perspective into the reaction pathways of 1,3-BD hydrogenation on monodisperse ensembles of Pt nanoparticle catalysts. Because of the nature of the SFG selection rules, the vibrational resonances that we observed are entirely due to the intermediates on the surface. The vibrational resonances can directly be correlated to the reactive intermediates and not spectrator species. We confirmed this by evacuating the reaction chamber and changing the reactor gas mixture to H$_2$/Ar immediately following the *in situ* measurement. The SFG signal completely reversed to the baseline measurement prior to performing the 1,3-BD hydrogenation reaction (not shown). We also confirmed that the SFG signal under reaction conditions was not related to the 1,3-BD-induced reordering of the PVP by exposing the catalysts to deuterated 1,3-BD and D$_2$ (not shown). After confirming that D$_2$ disorders the PVP in the

same manner as H$_2$, deuterated 1,3-BD exposed to the Pt nanoparticle catalysts showed negligible change in SFG signal. This is expected because methyl and methylene stretches of deuterated species are red-shifted to the range of 1900−2200 cm^{-1}.

Clear trends emerge from the kinetic selectivity and spectroscopy results. The ensembles of small nanoparticle catalysts produce more *n*-butane and *trans*-2-butene at the expense of total butenes and *cis*-2-butene, respectively, and the SFG signal originating from CH$_2$ resonances dramatically increases while the CH$_3$ resonances decrease. Figure 6 shows
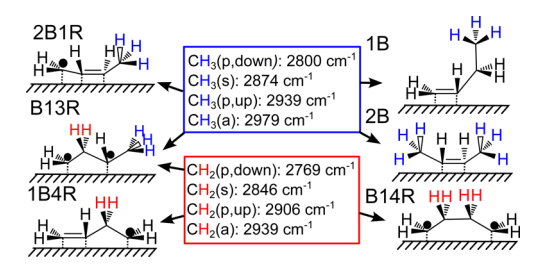

Figure 6. Six reaction intermediates produce SFG active methylene (red H) and methyl (blue H) vibrational stretches. Intermediates are designated using the IUPAC nomenclature with an "R" indicating a radical: 2-buten-1-yl (2B1R), butan-1,3-diyl (B13R), 1-butene (1B), and 2-butene (2B) produce bands associated with methyl resonances; B13R, 1-buten-4-yl (1B4R), and butan-1,4-diyl (B14R) produce bands associated with methylene resonances. The C−Pt bonds are located at the radical (●) and double bonded carbons. The methyl and methylene vibrations are designated with an s, a, p, up and down for symmetric, asymmetric, perturbed, away from the surface, and toward the surface, respectively. Note that *n*-butane can only originate from the B13R, 1B4R, or B14R intermediates (i.e., species with CH$_2$ vibrations).

the correspondence between the methyl (CH$_3$) and methylene (CH$_2$) vibrational bands and the likely adsorbed intermediates. Three of the proposed intermediates (1B4R, B13R, and B14R) will exhibit SFG-active CH$_2$ resonances, while four of the proposed intermediates (2B1R, B13R, 1-butene, and 2-butene) will exhibit SFG-active CH$_3$ resonances. SFG-active CH$_3$ resonances can also arise from a butan-2-yl or butan-1-yl species (a butan-2-yl is produced by H-addition to the C$_1$ atom of 1-butene, 2-butene, or B13R; a butan-1-yl radical is produced by H-addition to the C$_2$ atom of 1-butene or B13R); both of these intermediates are bound by a single σ-bond and are not expected to have a long lifetime on the surface of Pt in the presence of 1,3-BD.

The changes in the normalized SFG intensity ($\hat{I}_\nu$, eq 2) of CH$_2$(a)/CH$_3$(p,up) and CH$_3$(s) resonances at 2939 and 2874 cm^{-1}, respectively, versus Pt nanoparticle size are shown in Figure 7a. The SFG spectra on the 0.9 and 1.8 nm nanoparticles exhibit a large proportion of signal originating from the CH$_2$(a)/CH$_3$(p,up) vibrational bands. The 4.3 and 6.7 nm particles; however, have little signal originating from the CH$_2$(a)/CH$_3$(p,up) band. SFG intensities for the remaining resonances are given in Table S2 (Supporting Information). The reduced integral area of the CH$_3$(s) feature in Figure 7a for the small nanoparticles, despite the feature's apparent peak height in the SFG spectra, can be rationalized by the increased integral area of the two features located on either side of the CH$_3$(s) feature. SFG intensity is not simply a superposition of areas; instead, constructive interference of bands magnifies the combination of features by additional nonlinear terms. In
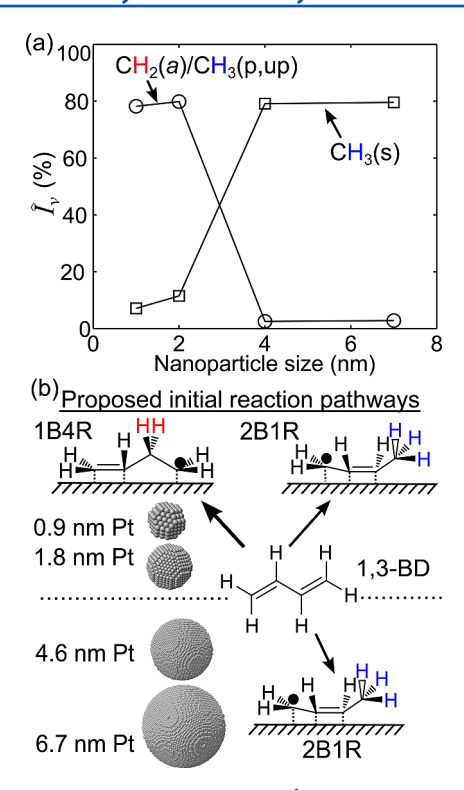
Figure 7. Normalized SFG intensity ($\hat{I}_\nu$, eq 2) for the $CH_2(a)$/$CH_3(p,up)$ (○) and $CH_3(s)$ (□) vibrational modes as a function of nanoparticle size. $\hat{I}_\nu$ is a function of orientation/order and concentration. Small nanoparticles have an increased contribution to the SFG signal from the $CH_2(a)$/$CH_3(p,up)$ modes, whereas large particles are dominated by the $CH_3(s)$ mode. The proposed initial reaction pathways for the 0.9 and 1.8 nm Pt nanoparticles (above dotted line) and 4.6 and 6.7 nm Pt nanoparticles (below dotted line) are shown below. The methylene and methyl groups that exhibit SFG signal are highlighted in red and blue. The small nanoparticles exhibit methylene (CH_2) stretches that indicate the presence of the 1B4R intermediate. This pathway leads to n-butane. The pathway starting with 2B1R leads predominantly to butenes.

contrast, the $CH_2(a)$/$CH_3(p,up)$ feature is on the edge of the spectral profile. Note that $\hat{I}_\nu$ is a function of orientation/order and concentration. Therefore, we cannot directly correlate these vibrational signatures to a quantitative assessment of the reaction intermediates. This qualitative assessment can, however, correlate the likely reaction intermediates and reaction pathways with nanoparticle size.

In view of Figure 7a and the DFT predictions[7−9] discussed previously, we infer from the magnitude of the $CH_3(s)$ band that 1,3-BD hydrogenation on the large particles favors the 2B1R pathway. Even though the activation barrier from 1,3-BD to 2B1R and 1,3-BD to 1B4R was proposed to be nearly equal, 2B1R is more thermodynamically stable on Pt(111) by ~17 kJ/mol.[8] Moreover, the reaction pathway through the π-bonded intermediate is considered to be orders of magnitude more rapid than on the di-σ bonded counterpart during ethylene and propylene hydrogenation[14,29,31] and H-addition to a terminal carbon was shown to be three times more favorable than an internal carbon.[38] Therefore, we attribute the $CH_3(s)$ mode at 2874 cm^{-1} to the 2B1R intermediate. The 2B1R intermediate will also produce a $CH_3(a)$ mode and perturbed variations (as discussed in the Supporting Information) but will not yield any CH_2 activity. We assign the CH_2 resonance activity at 2846, 2906, and 2939 cm^{-1} (determined via the

model) to the 1B4R and/or B13R intermediate(s). Both of these intermediates are along the pathway to n-butane. From a thermodynamic perspective of the adsorbates on a Pt(111) surface, the active CH_2 modes could be attributed to the 1B4R intermediate, which is predicted to be 6 kJ/mol more stable than the B13R;[8] however, from a kinetic perspective, the second hydrogenation step from the 2B1R to B13R is more favorable than the pathway from 1B4R to B13R. Thus, the n-butane formed on the large particles (and Pt bulk surfaces) corresponds to the pathway through the B13R intermediate. The low CH_2 band intensity observed on the large particles correlates with the low selectivity to n-butane. The low intensity may also suggest that the B13R intermediate does not have a long lifetime on the surface. In contrast to the large nanoparticles, we cannot use the Pt(111)-based DFT energetics to argue plausible reaction intermediates for the small nanoparticle catalysts. However, we rationalize the 30% increase in n-butane selectivity based on the same set of reaction intermediates.

The increase in CH_2 resonances (i.e., bands at 2846, 2906, and 2939 cm^{-1}) confirms that the ensembles of small nanoparticle catalysts provide favorable pathways to n-butane. The decline in the production of 1-butene is not due to further hydrogenation of 1-butene on the surface, since the reaction was performed under excess 1,3-BD, as discussed previously. Instead, plausible explanations arise from changes in the potential energy pathways on the surface, which comprise of a destabilized 2B1R intermediate, a stabilized 1B4R intermediate, a stabilized B13R intermediate, a destabilized transition state between the 1B4R and B13R intermediates, or a destabilized transition state between the 2B1R and B13R intermediates (cf. Figure 1). The decrease in CH_3 vibrational bands (Figure 7a) and the fact that selectivity toward 2-butenes changes only slightly indicates that the change is not due to a destabilized 2B1R intermediate. A decreased surface lifetime of the 2B1R species at the expense of a stabilized B13R intermediate (change in quasi-equilibrium) would not necessarily change the concentration of CH_3 vibrational modes but simply provide additional CH_2 modes, which is not consistent with trends shown in Figure 7a. It is well-known that small nanoparticles exhibit an increase in edge/step and corner sites at the expense of terrace sites.[10,39] Reduced atomic coordination results in an improved molecule−particle chemical interaction via shifts in the d-band center toward the Fermi level, which increases the number of empty antibonding states. Moreover, a higher d-band center makes the surface more reactive by lowering the transition state energies.[13,16,40,41] The presence of low-coordination sites will alter the stability of metallocycle binding geometries (like 1B4R and B13R) and transition states by reducing strain of the geometric configuration that would not be stable on a terrace.[39,42] This would suggest that the presence of low-coordination sites promotes the pathway proceeding via H-insertion at the internal carbon, which leads to the metallocycle 1B4R. Thus, we believe that the observed CH_2 signal originates from the 1B4R species.

■ CONCLUSION

Understanding how to control the reaction pathways that lead to different product distributions is critical to rational design of heterogeneous catalysts. We have shown using colloidally synthesized monodisperse nanoparticle distributions that the size of Pt nanoparticle catalysts impacts the product distribution in 1,3-butadiene hydrogenation. Two parallel

reaction pathways lead to the full and partial hydrogenation products and the nanoparticle size impacts the kinetic preference toward each pathway. Ensembles of Pt nanoparticle catalysts of 0.9 and 1.8 nm promote a 30 and 20% increase in the full hydrogenation (n-butane) of 1,3-butadiene, respectively, in comparison to 4.6 and 6.7 nm Pt catalysts. Formation of n-butane occurs at the expense of 1-butene rather than 2-butene products. *In situ* SFG vibrational spectroscopy was used to monitor the adsorbed reaction intermediates on Pt nanoparticles with the capping ligand intact, under working conditions identical to those of the kinetic experiments. The results indicate that the 0.9 and 1.8 nm Pt catalysts provide adsorption sites (e.g., low coordination sites) that facilitate H-insertion at an internal carbon (1B4R), in addition to H-insertion at the terminal carbon (2B1R), whereas the 4.6 and 6.7 nm Pt catalysts favor H-insertion at the terminal carbon as observed on Pt bulk materials.

■ ASSOCIATED CONTENT

Ⓢ Supporting Information

Descriptions of the nanoparticle synthesis; SFG spectra of an ensemble of 2 nm Pt nanoparticles capped with PVP exposed to different atmospheres at 75 °C (Figure S1); discussion of vibrational bands at 2680, 2769, 2800, and 2979 cm^{-1}; fitting parameters for the SFG spectra presented in the main text and previous discussion (Table S1); normalized intensities of bands from the model SFG spectra (Table S2). This material is available free of charge via the Internet at http://pubs.acs.org.

■ AUTHOR INFORMATION

Corresponding Author

*Tel 510-642-4053; Fax 510-643-9668; e-mail somorjai@berkeley.edu (G.A.S.), wmichalak@gmail.com (W.D.M.).

Notes

The authors declare no competing financial interest.

■ ACKNOWLEDGMENTS

■ REFERENCES

(1) Oudar, J.; Pinol, S.; Pradier, C. M.; Berthier, Y. *J. Catal.* **1987**, *107*, 445.
(2) Pradier, C. M.; Margot, E.; Berthier, Y.; Oudar, J. *Appl. Catal.* **1988**, *43*, 177.
(3) Primet, M.; Elazhar, M.; Guenin, M. *Appl. Catal.* **1990**, *58*, 241.
(4) Yoon, C. H.; Yang, M. X.; Somorjai, G. A. *Catal. Lett.* **1997**, *46*, 37.
(5) Massardier, J.; Bertolini, J. C.; Ruiz, P.; Delichere, P. *J. Catal.* **1988**, *112*, 21.
(6) Sarkany, A.; Stefler, G.; Hightower, J. W. *Appl. Catal., A* **1995**, *127*, 77.
(7) Delbecq, F.; Loffreda, D.; Sautet, P. *J. Phys. Chem. Lett.* **2010**, *1*, 323.
(8) Valcarcel, A.; Clotet, A.; Ricart, J. M.; Delbecq, F.; Sautet, P. *J. Phys. Chem. B* **2005**, *109*, 14175.
(9) Vigne, F.; Haubrich, J.; Loffreda, D.; Sautet, P.; Delbecq, F. *J. Catal.* **2010**, *275*, 129.
(10) Somorjai, G. A. *Introduction to Surface Chemistry and Catalysis*, 2nd ed.; Wiley: Hoboken, NJ, 2010.
(11) McCrea, K. R.; Somorjai, G. A. *J. Mol. Catal A: Chem.* **2000**, *163*, 43.
(12) Hammer, B.; Nielsen, O. H.; Norskov, J. K. *Catal. Lett.* **1997**, *46*, 31.
(13) Norskov, J. K.; Abild-Pedersen, F.; Studt, F.; Bligaard, T. *Proc. Natl. Acad. Sci. U. S. A.* **2011**, *108*, 937.
(14) Zaera, F. *Appl. Catal., A* **2002**, *229*, 75.
(15) Singh, U. K.; Vannice, M. A. *Appl. Catal., A* **2001**, *213*, 1.
(16) Kleis, J.; Greeley, J.; Romero, N. A.; Morozov, V. A.; Falsig, H.; Larsen, A. H.; Lu, J.; Mortensen, J. J.; Dulak, M.; Thygesen, K. S.; Norskov, J. K.; Jacobsen, K. W. *Catal. Lett.* **2011**, *141*, 1067.
(17) Alayoglu, S.; Aliaga, C.; Sprung, C.; Somorjai, G. A. *Catal. Lett.* **2011**, *141*, 914.
(18) Pushkarev, V.; Musselwhite, N.; An, K.; Alayoglu, S.; Somorjai, G. A. *Nano Lett.* **2012**, *12*, 5196.
(19) Rioux, R. M.; Song, H.; Hoefelmeyer, J. D.; Yang, P.; Somorjai, G. A. *J. Phys. Chem. B* **2005**, *109*, 2192.
(20) Shen, Y. R. *The Principles of Nonlinear Optics*; Wiley: New York, 1984.
(21) Yang, M. C.; Chou, K. C.; Somorjai, G. A. *J. Phys. Chem. B* **2004**, *108*, 14766.
(22) Lambert, A. G.; Davies, P. B.; Neivandt, D. J. *Appl. Spectrosc. Rev.* **2005**, *40*, 103.
(23) Aliaga, C.; Tsung, C. K.; Alayoglu, S.; Komvopoulos, K.; Yang, P. D.; Somorjai, G. A. *J. Phys. Chem. C* **2011**, *115*, 8104.
(24) Himmelhaus, M.; Eisert, F.; Buck, M.; Grunze, M. *J. Phys. Chem. B* **2000**, *104*, 576.
(25) Fletcher, R.; Powell, M. J. D. *Comput. J.* **1963**, *6*, 163.
(26) Ugray, Z.; Lasdon, L.; Plummer, J.; Glover, F.; Kelly, J.; Marti, R. *Informs J Comput* **2007**, *19*, 328.
(27) Somorjai, G. A.; Park, J. Y. *Angew. Chem., Int. Ed.* **2008**, *47*, 9212.
(28) Krier, J. M.; Michalak, W. D.; Baker, L. R.; An, K.; Komvopoulos, K.; Somorjai, G. A. *J. Phys. Chem. C* **2012**, *116*, 17540.
(29) Cremer, P.; Stanners, C.; Niemantsverdriet, J. W.; Shen, Y. R.; Somorjai, G. *Surf. Sci.* **1995**, *328*, 111.
(30) Cremer, P. S.; Su, X. C.; Shen, Y. R.; Somorjai, G. A. *J. Am. Chem. Soc.* **1996**, *118*, 2942.
(31) Cremer, P. S.; Su, X. C.; Shen, Y. R.; Somorjai, G. A. *J. Phys. Chem.* **1996**, *100*, 16302.
(32) Cremer, P. S.; Su, X. C.; Shen, Y. R.; Somorjai, G. *J. Chem. Soc., Faraday Trans.* **1996**, *92*, 4717.
(33) Bratlie, K. M.; Somorjai, G. A. *J. Phys. Chem. C* **2007**, *111*, 6837.
(34) Manner, W. L.; Bishop, A. R.; Girolami, G. S.; Nuzzo, R. G. *J. Phys. Chem. B* **1998**, *102*, 8816.
(35) Chesters, M. A.; Gardner, P.; Mccash, E. M. *Surf. Sci.* **1989**, *209*, 89.
(36) Lee, K.; Zaera, F. *J. Phys. Chem. B* **2005**, *109*, 2745.
(37) Wang, H. F.; Gan, W.; Lu, R.; Rao, Y.; Wu, B. H. *Int. Rev. Phys. Chem.* **2005**, *24*, 191.
(38) Klein, R.; Scheer, M. D.; Waller, J. G. *J. Phys. Chem.* **1960**, *64*, 1247.
(39) Coq, B.; Figueras, F. *Coord. Chem. Rev.* **1998**, *178*, 1753.
(40) Kitchin, J. R.; Norskov, J. K.; Barteau, M. A.; Chen, J. G. *Phys. Rev. Lett.* **2004**, *93*, 046101.
(41) Schnur, S.; Gross, A. *Phys. Rev. B* **2010**, *81*, 033402.
(42) Hammer, B.; Norskov, J. K. *Adv. Catal.* **2000**, *45*, 71.
(43) Fosser, K. A.; Kang, J. H.; Nuzzo, R. G.; Woll, C. *J. Chem. Phys.* **2007**, *126*, 194707.
(44) Yamamoto, M.; Sakurai, Y.; Hosoi, Y.; Ishii, H.; Ito, E.; Kajikawa, K.; Ouchi, Y.; Seki, K. *Surf. Sci.* **1999**, *427–28*, 388.